Sun *et al.*
Chinese Journal of Mechanical Engineering (2022) 35:94
https://doi.org/10.1186/s10033-022-00768-3

Chinese Journal of Mechanical Engineering

ORIGINAL ARTICLE

Open Access

Resolution Enhancement in Ultrasonic TOFD Imaging by Combining Sparse Deconvolution and Synthetic Aperture Focusing Technique (Sparse-SAFT)

Xu Sun, Li Lin and Shijie Jin*

Abstract

The shallow subsurface defects are difficult to be identified and quantified by ultrasonic time-of-flight diffraction (TOFD) due to the low resolution induced by pulse width and beam spreading. In this paper, Sparse-SAFT is proposed to improve the time resolution and lateral resolution in TOFD imaging by combining sparse deconvolution and synthetic aperture focusing technique (SAFT). The mathematical model in the frequency domain is established based on the l_1 and l_2 norm constraints, and the optimization problem is solved for enhancing time resolution. On this basis, SAFT is employed to improve lateral resolution by delay-and-sum beamforming. The simulated and experimental results indicate that the lateral wave and tip-diffracted waves can be decoupled with Sparse-SAFT. The shallow subsurface defects with a height of 3.0 mm at the depth of 3.0 mm were detected quantitatively, and the relative measurement errors of flaw heights and depths were no more than 10.3%. Compared to conventional SAFT, the time resolution and lateral resolution are enhanced by 72.5 and 56% with Sparse-SAFT, respectively. Finally, the proposed method is also suitable for improving resolution to detect the defects beyond dead zone.

Keywords: Time resolution, Lateral resolution, Time-of-flight diffraction (TOFD), Sparse deconvolution, Synthetic aperture focusing technique (SAFT), Sparse-SAFT

1 Introduction

Ultrasonic testing is widely used to inspect material properties and estimate defects quantitatively [1, 2]. Time-of-flight diffraction (TOFD) is an ultrasonic testing technique with high inspection speed and accurate size measurement, and B-scan image is the common mode for presenting detection results [3–7]. However, ultrasonic signals are received in the wide range due to beam spreading, inducing that the tip-diffracted waves are displayed as hyperbolic arcs in the B-scan image. Meanwhile, the detectable range by TOFD is more than 7.0 mm in general [8]. The shallow subsurface defects located in dead zone are hard to be identified because of the superposition between lateral wave and tip-diffracted waves [8–10]. Therefore, it is necessary to improve lateral resolution and time resolution in TOFD detection image by combining signal processing techniques.

The deconvolution techniques are beneficial to improving time resolution. Compared to conventional Weiner filter, the Weiner filter followed by autoregressive spectral extrapolation is more suitable to separate overlapped signals by the specific combination of multiple frequency windows [11, 12]. This method was employed by ultrasonic TOFD technique to quantitatively evaluate the near-surface notch with 3.0 mm depth [13]. In contrast, the sparsity reflecting the limited number of spikes in reflection sequence is the powerful prior information

*Correspondence: jinshijie@dlut.edu.cn

School of Materials Science and Engineering, Dalian University of Technology, Dalian, China

in ultrasonic testing. Some sparsity-based methods are developed to obtain the sparse signals with high time resolution by introducing l_1-norm constraint rather than extending the frequency band [14–19]. For example, the sparsity constraint is imposed on the overlapped TOFD signals from defect, realizing the improvement of time resolution and the quantitative estimation of 0.5 μs time difference [18].

The delay-and-sum (DAS) beamforming algorithms, e.g., synthetic aperture focusing technique (SAFT), are well-known for improving the lateral resolution in ultrasonic imaging [20]. Meanwhile, SAFT is employed to enhance signal-to-noise ratio (SNR) and quantify defects by imaging the ultrasonic signals with low directivity [21–26]. Based on the relative position between defect and TOFD probes [27], the lateral resolution of B-scan images is improved to identify defects by using SAFT. On this basis, the combination of SAFT and phase coherence imaging (PCI) provides better lateral resolution and SNR level [28]. It should be noted that the methods mentioned above focus on the enhancement of lateral resolution or time resolution. When the to-be-detected defects are located in the dead zone, the ideal lateral resolution and time resolution are difficult to be obtained by the single method simultaneously. It is necessary to combine different methods for realizing resolution enhancement.

In this paper, Sparse-SAFT is proposed to enhance the resolution in TOFD imaging. First, the sparsity of reflection sequence is applied to processing the TOFD signals. Then, the l_1 and l_2 norm constraints are combined to construct the objective function in the frequency domain, weakening the influence of the pulse width and beam spreading of original signals. Finally, SAFT is used to obtain the high-resolution image, and to size the defects in dead zone. Section 2 presents the theories of TOFD inspection and Sparse-SAFT. The simulated and experimental results are described in Section 3. Section 4 is the discussion, and the conclusions are presented in Section 5.

2 Theories

2.1 TOFD Inspection

The schematic diagram of ultrasonic TOFD inspection is presented in Figure 1(a), where the transmitter (T) and receiver (R) are a pair of probes connected with the wedges having the same angle [28–31]. The received signal $y(n)$ is modeled as

$$y(n) = w(n) * r(n) + n(n), \tag{1}$$

where * represents convolution, $w(n)$ is input pulse, $r(n)$ is reflection sequence, and $n(n)$ is the noise.

The B-scan is obtained by using the TOFD probes scanning with a step of Δs from position 1 to position M, where the probe center spacing (PCS) is $2S$. The point coordinates of transmitter and receiver at position i ($1 \le i \le M$) are respectively defined as ($i\Delta s$, 0) and ($i\Delta s+2S$, 0), and the corresponding received signal is denoted as $y^i(n)$. Therefore, the B-scan image, i.e., signal matrix $\boldsymbol{B}_{raw}=[y^1(n), \ldots, y^i(n), \ldots, y^M(n)]$, is consisted of M-number A-scan signals, as schematically presented in Figure 1(b).

As shown in Figure 1(b), the received signal $y^i(n)$ contains lateral wave and tip-diffracted waves. There is a near-surface dead zone with a depth of D due to the pulse width of lateral wave, as given by

$$D = [c_l^2(\frac{t_p}{2})^2 + c_l S t_p]^{1/2}, \tag{2}$$

where t_p is the pulse width of lateral wave, and c_l is the longitudinal wave velocity in specimen.

The dead zone leads to the difficulty in calculating the defect depth d and height h with Eqs. (3) and (4).

$$d = \sqrt{(S + c_l \Delta t_1/2)^2 - S^2}, \tag{3}$$

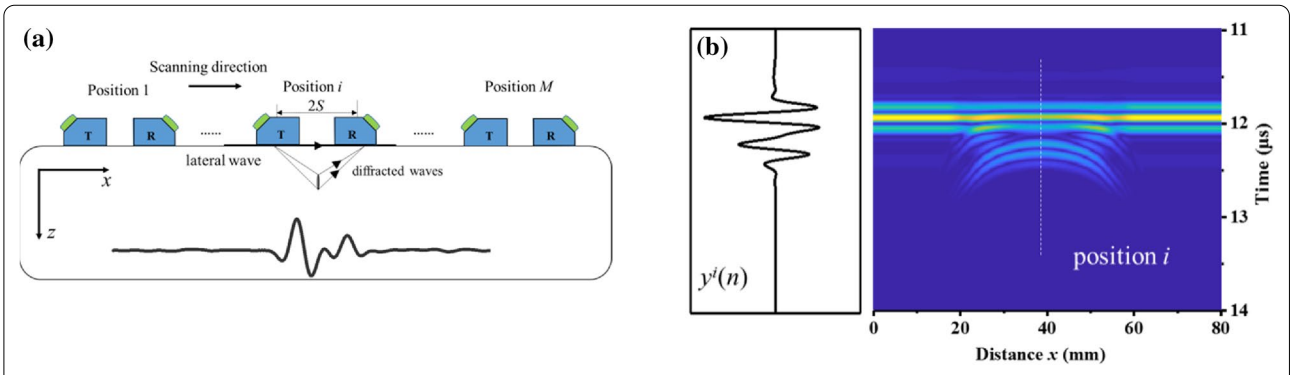

Figure 1 Schematic diagrams of ultrasonic TOFD inspection and B-scan image: (**a**) ultrasonic TOFD inspection, (**b**) A-scan signal at position *i* and B-scan image

$$h = \sqrt{(S + c_l \Delta t_2/2)^2 - S^2} - d, \tag{4}$$

where Δt_1 and Δt_2 are the time differences between the lateral wave and the diffracted waves from upper and lower tips, respectively.

In addition, the diffracted waves from defect tips are displayed as hyperbolic arcs in the B-scan image presented in Figure 1(b). The low lateral resolution influences the quantitative estimation of defect depth and size.

2.2 Sparse-SAFT

In this paper, Sparse-SAFT is proposed to enhance resolution by combining sparse deconvolution and SAFT. First, the TOFD inspection model is converted into the mathematical model in the frequency domain to construct an objective function.

The expression of Eq. (1) in the frequency domain is given by

$$\boldsymbol{Y}(f) = \boldsymbol{W}(f)\boldsymbol{R}(f) + \boldsymbol{N}(f), \tag{5}$$

where $\boldsymbol{Y}(f)$, $\boldsymbol{R}(f)$, $\boldsymbol{W}(f)$, and $\boldsymbol{N}(f)$ are the corresponding frequency spectrums of $y(n)$, $r(n)$, $w(n)$, and $n(n)$, respectively.

The frequency spectrum $\boldsymbol{R}(f)$ is estimated by Wiener filter.

$$\boldsymbol{R}(f) = \frac{\boldsymbol{Y}(f)\boldsymbol{W}^*(f)}{|\boldsymbol{W}(f)|^2 + Q}, \tag{6}$$

where $\boldsymbol{W}^*$ is the conjugate of $\boldsymbol{W}$, the noise desensitizing factor Q is often approximated as $0.01\max(|\boldsymbol{W}(f)|^2)$ [11, 19].

Meanwhile, the discrete reflection sequence $r(n)$ can also be expressed as Eq. (7) [11, 19].

$$r(n) = \sum_{i=1}^{N} r_i \delta(n - t_i), \tag{7}$$

where r_i is the amplitude at the ith point; N is the length of $r(n)$, and t_i is the corresponding time interval between the ith point and the 1st point.

The expression of Eq. (7) in the frequency domain is given by

$$\boldsymbol{R}(f) = \sum_{k=1}^{N} [r(t_k)\cos(2\pi f t_k)] - j\sum_{k=1}^{N} [r(t_k)\sin(2\pi f t_k)]. \tag{8}$$

Therefore, Eq. (9) is deduced by combining Eqs. (6) and (8).

$$\begin{aligned} &\frac{\boldsymbol{Y}(f)\boldsymbol{W}^*(f)}{|\boldsymbol{W}(f)|^2 + Q} \\ &= \sum_{k=1}^{N} [r(t_k)\cos(2\pi f t_k)] - j\sum_{k=1}^{N} [r(t_k)\sin(2\pi f t_k)]. \end{aligned} \tag{9}$$

Eq. (9) is rearranged as Eq. (10) according to the equivalence of the real parts and imaginary parts on both sides.

$$\boldsymbol{A}_{2N\times 1} = \boldsymbol{C}_{2N\times N}\boldsymbol{R}_{N\times 1}, \tag{10}$$

where $\boldsymbol{A}$=[real($\boldsymbol{R}(f_1)$),..., real($\boldsymbol{R}(f_N)$), img($\boldsymbol{R}(f_1)$), ..., img($\boldsymbol{R}(f_N)$)]; $\boldsymbol{C}$=[cos(2πf_1t_1), ... cos(2πf_1t_N),... ,cos(2πf_Nt_1), ..., cos(2πf_Nt_N), sin(2πf_1t_1), ...sin(2πf_1t_N), ..., sin(2πf_Nt_1), ..., sin(2πf_Nt_N)]; $\boldsymbol{R}$=[$r(t_1)$,...,$r(t_N)$]. real{} is the real part, and img{} is the imaginary part. More details are described in Ref. [13]. It is obvious that the problem given by Eq. (10) has multiple solutions.

Subsequently, l_1 norm constraint is imposed on $\boldsymbol{R}$ based on the sparsity of reflection sequence. The high-resolution signal can be obtained by solving the following problem.

$$\min\|\boldsymbol{R}\|_1 \text{ s.t. } \boldsymbol{A} = \boldsymbol{C}\boldsymbol{R}. \tag{11}$$

The constraint problem in Eq. (11) is transformed into the unconstraint problem in Eq. (12) by combining l_2 and l_1 norm constraints.

$$\boldsymbol{X}(n) = \arg\min_{R}\{\|\boldsymbol{C}\boldsymbol{R} - \boldsymbol{A}\|_2 + \mu\|\boldsymbol{R}\|_1\}, \tag{12}$$

where μ is the regularization parameter.

On this basis, the interior-point method [32] is employed to solve Eq. (12), and the sparse signal matrix $\boldsymbol{B}_{\text{sparse}}$ is obtained by processing every A-scan signal in matrix $\boldsymbol{B}_{\text{raw}}$.

$$\boldsymbol{B}_{\text{sparse}} = [X^1(n), ..., X^i(n), ..., X^M(n)]. \tag{13}$$

Finally, SAFT is implemented on the matrix $\boldsymbol{B}_{\text{sparse}}$ to improve lateral resolution. The delay time ΔT_i corresponding to position i and an arbitrary point (x, z) in the region of interest is given by

$$\begin{aligned} \Delta T_i(x,z) =& (\sqrt{(i\Delta s - x)^2 + z^2} \\ &+ \sqrt{(i\Delta s - x + 2S)^2 + z^2} \\ &- 2\sqrt{S^2 + z^2})/c_l. \end{aligned} \tag{14}$$

The DAS calculation is performed on every processed A-scan signal $X^i(n)$ to obtain the reconstructed image $\boldsymbol{B}_{\text{Sparse-SAFT}}(x, z)$.

$$\boldsymbol{B}_{\text{Sparse - SAFT}}(x,z) = \sum_{i=1}^{M} X^i(\Delta T_i(x,z)). \tag{15}$$

The flow chart of Sparse-SAFT is presented in Figure 2.

3 Simulation and Experiments

3.1 Simulation

Figure 3 presents the schematic diagram of the carbon steel model established in the CIVA software platform, and the longitudinal wave velocity c_l in carbon steel is equal to 5890 m/s. The shallow subsurface cracks #1–#3 with height h = 3.0 mm were set at the depth d =3.0, 3.5 and 4.0 mm, respectively. TOFD inspection was implemented by using a pair of probes with 5 MHz center frequency, 70° refraction angle, and 30.0 mm PCS. Therefore, the depth of dead zone was 6.1 mm for the t_p=0.4 μs.

Figures 4(a) and 5(a) present the original B-scan image and A-scan signals corresponding to the three cracks, respectively. On the one hand, the time differences between lateral wave and tip-diffracted waves are difficult to be determined due to signal superposition. On the other hand, the beam spreading induces

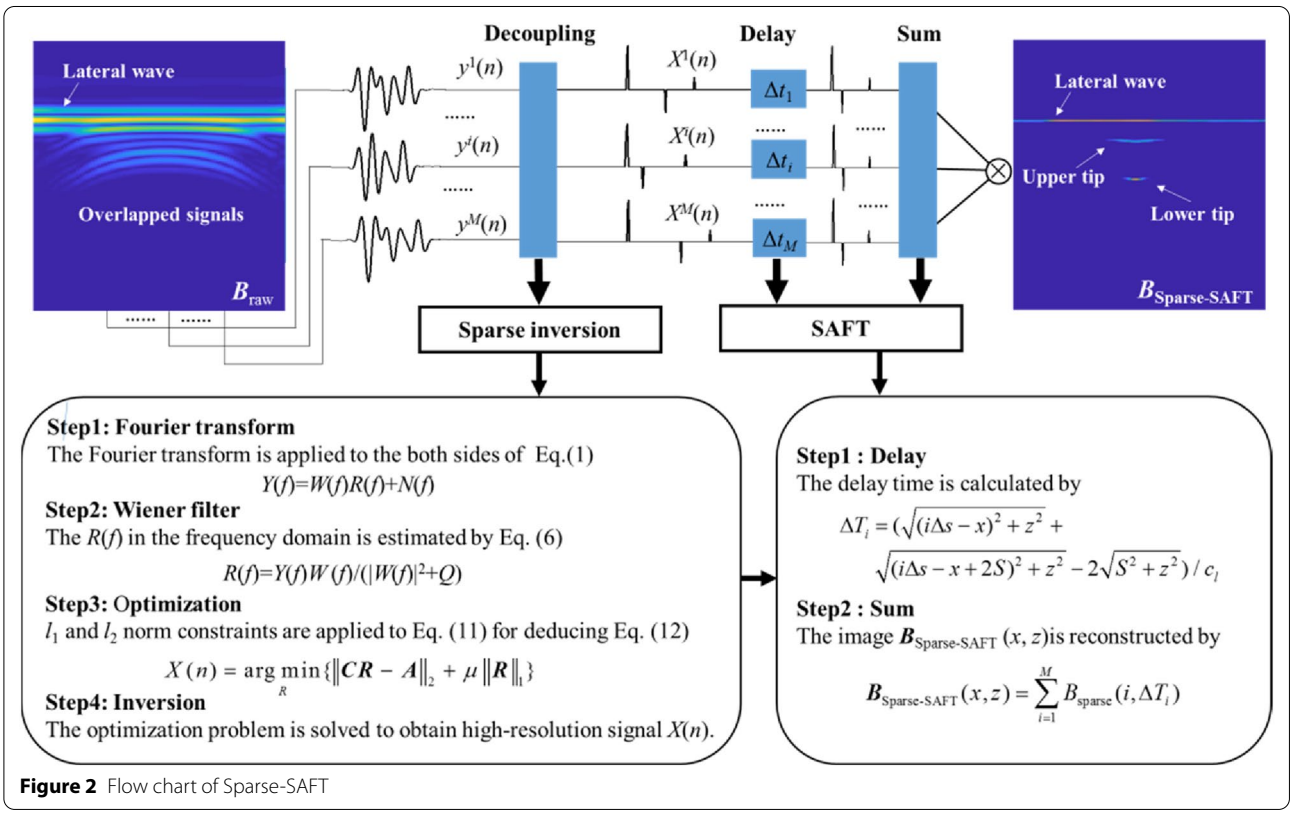

Figure 2 Flow chart of Sparse-SAFT

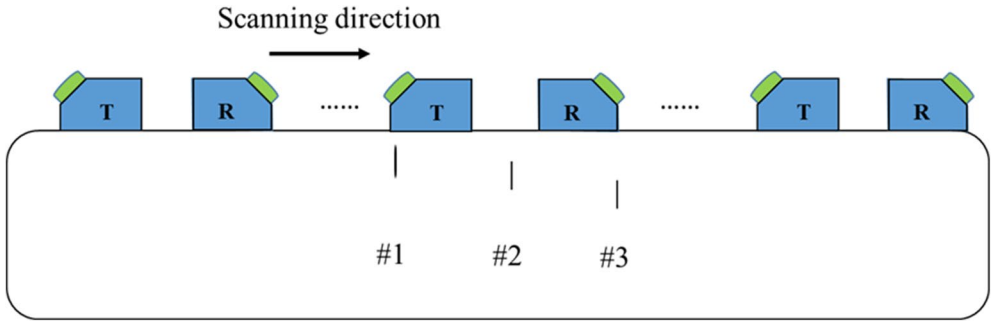

Figure 3 Schematic diagram of detecting shallow subsurface cracks with ultrasonic TOFD

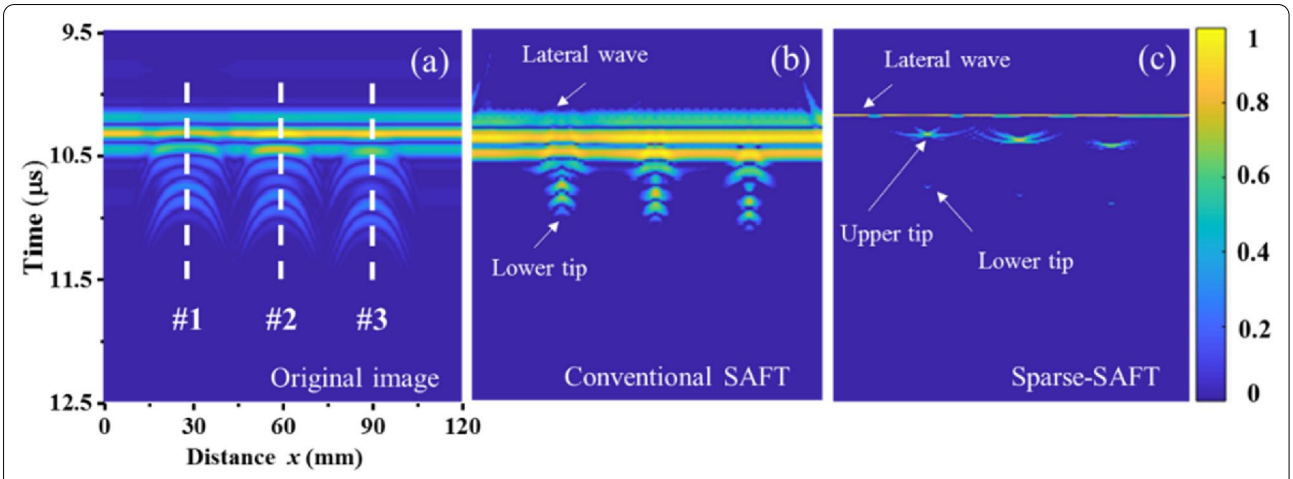

Figure 4 Original image and reconstructed images by simulation: (**a**) original B-scan image, (**b**) reconstructed image by conventional SAFT, (**c**) reconstructed image by Sparse-SAFT

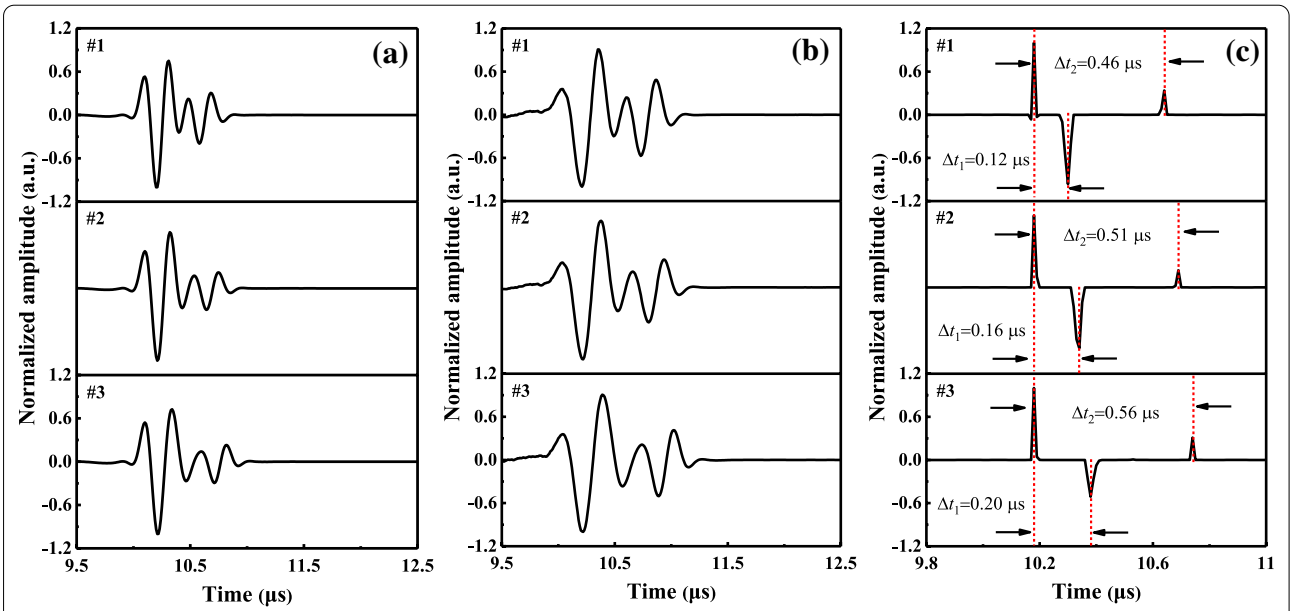

Figure 5 A-scan signals corresponding to the three cracks in different images: (**a**) in the original image, (**b**) in the reconstructed image by conventional SAFT, (**c**) in the reconstructed image by Sparse-SAFT

the tip-diffracted waves presented as hyperbolic arcs in the image, influencing the identification of defect characteristics.

Figures 4(b) and 5(b) show the reconstructed image and A-scan signals by using conventional SAFT, respectively. The lateral resolution is enhanced in comparison with Figure 4(a), but there is no obvious improvement in time resolution. The arrival times of lateral wave and tip-diffracted waves are unable to be obtained from the image and A-scan signals.

On this basis, the Sparse-SAFT was employed to process the signal matrix $\boldsymbol{B}_{\text{raw}}$. The frequency spectrum $\boldsymbol{R}(f)$ was estimated by Wiener filter, and norm constraints were imposed based on the sparsity for deducing the optimization problem given by Eq. (12). Subsequently, the interior-point method was applied to solve the problem, obtaining the sparse signal matrix $\boldsymbol{B}_{\text{sparse}}$. Finally, SAFT was implemented by DAS calculation to reconstruct the high-resolution image $\boldsymbol{B}_{\text{Sparse-SAFT}}$. Figures 4(c) and 5(c) present the reconstructed image and A-scan signals by Sparse-SAFT. Compared to Figures 4(a) and (b), the time resolution and lateral resolution in Figure 4(c) are both improved

Table 1 Calculated crack depths and heights and relative errors by Sparse-SAFT

Defect number	*d* (mm)	Error (%)	*h* (mm)	Error (%)
#1	3.28	9.3	3.24	8.0
#2	3.79	8.3	3.09	3.0
#3	4.24	6.0	2.98	0.7

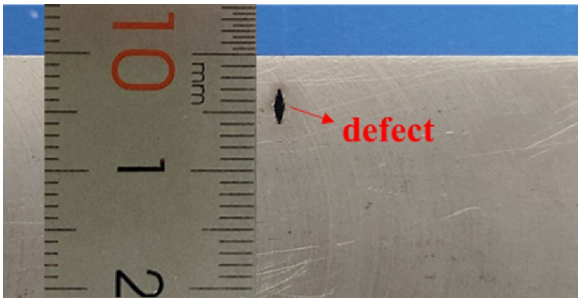

Figure 6 Carbon steel specimen with an artificial defect machined at the depth of 3.0 mm

significantly, and the lateral wave and tip-diffracted waves are distinguished clearly.

Table 1 lists the crack depths and heights calculated with Eqs. (3) and (4) based on the time differences Δt_1 and Δt_2 read from Figure 5(c). The relative measurement errors are no more than 9.3%.

3.2 Experiments

Figure 6 presents the carbon steel specimen used for experiments. An artificial defect with a height of 3.0 mm was machined at the depth of 3.0 mm. The longitudinal wave velocity c_l was 5890 m/s. Ultrasonic TOFD inspection was implemented using a pair of probes with 5.0 MHz center frequency and 30.0 mm PCS. Therefore, the defect was located in the dead zone (D=6.1mm).

Figure 7 presents the original B-scan image and the reconstructed images by conventional SAFT and Sparse-SAFT. The A-scan signals corresponding to the defect in reconstructed images are shown in Figure 8. The lateral resolution is improved by conventional SAFT in comparison with the original image. However, there is no enhancement in time resolution, as shown in Figure 8(a). In contrast, the time resolution and lateral resolution are both significantly improved in the reconstructed image by Sparse-SAFT. Figure 8(b) demonstrates that the lateral wave and tip-diffracted waves are feasible to identify from the decoupled signals. The flaw depth (d=2.83 mm) and height (h=3.31 mm) are calculated with Eqs. (3) and (4) by the time differences Δt_1 and Δt_2 in Figure 8(b). The relative measurement errors are no more than 10.3%.

4 Discussion

The low time resolution and lateral resolution restrict the identification and quantitation of shallow subsurface defects from TOFD images. In this paper, the l_1 and l_2 norm constraints are introduced to solving the frequency-domain optimization problem for improving time resolution, and SAFT is employed to enhance

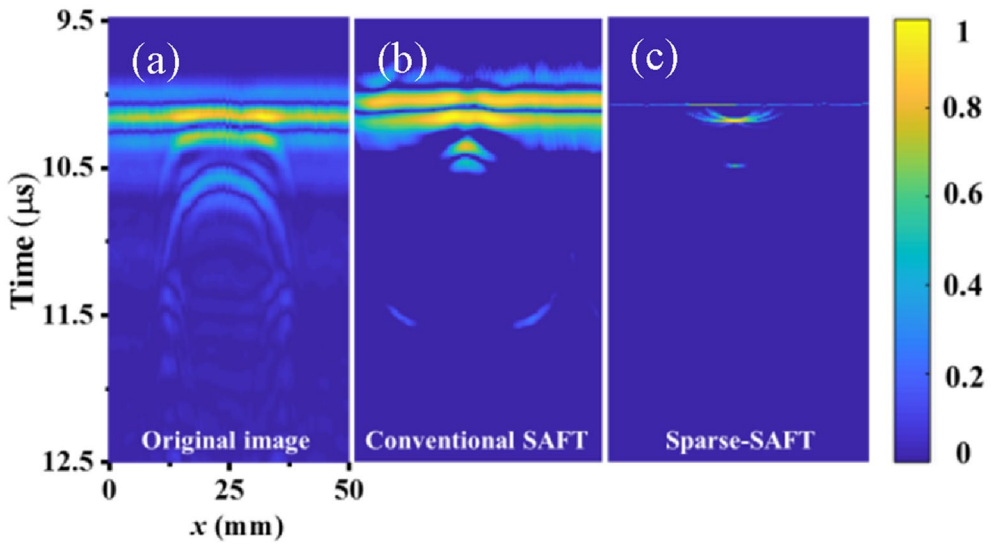

Figure 7 Original image and reconstructed images by experiments: (**a**) original B-scan image, (**b**) reconstructed image by conventional SAFT, (**c**) reconstructed image by Sparse-SAFT

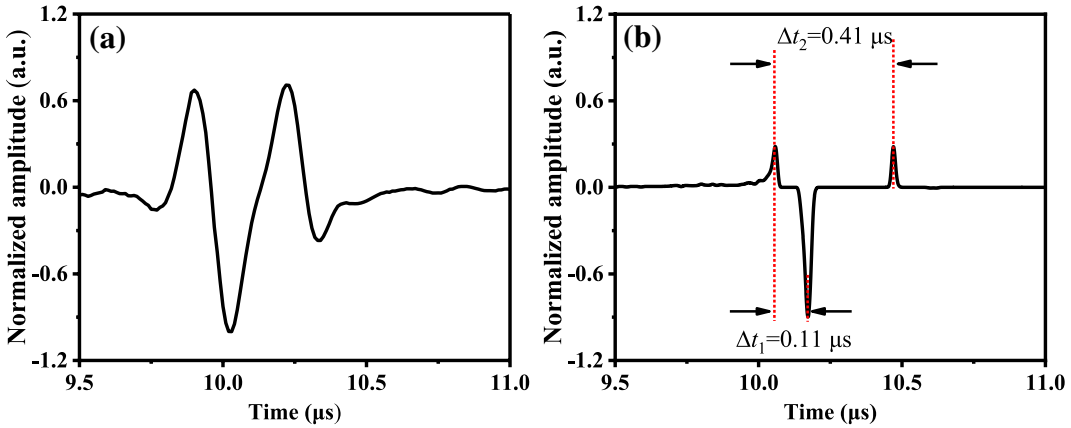

Figure 8 A-scan signals corresponding to the defect in different experimental reconstructed images: (**a**) in the image by conventional SAFT, (**b**) in the image by Sparse-SAFT

lateral resolution by DAS calculation. It should be noted that the DAS images by conventional SAFT are reconstructed based on the original ultrasonic A-scan signals. The signals with wide pulse-width contain redundant information of non-defects, resulting in the overlapping of lateral wave and tip-diffracted waves. There is no improvement in time resolution by conventional SAFT, and the arrival times of the lateral wave and tip-diffracted waves are hard to be determined from the reconstructed images. In contrast, Sparse-SAFT is proposed to decouple overlapped signals and reconstruct images. The pulse widths of lateral wave and tip-diffracted waves are greatly reduced. In addition, the improvement of time resolution for array signals is beneficial to the enhancement of lateral resolution in reconstructed images with the delay-and-sum beamforming method, e.g., SAFT and TFM [33]. The introduction of sparse deconvolution increases the focusing effects of SAFT. The reconstructed images by Sparse-SAFT contain less redundant information, realizing the identification and location of near-surface defects. Therefore, the combination of sparse deconvolution and SAFT is helpful for enhancing the time and lateral resolution of ultrasonic TOFD images and has higher resolution in comparison with conventional SAFT.

Experimental results demonstrate that Sparse-SAFT has the ability to realize the resolution enhancement in TOFD imaging as shown in Figures 7 and 8. On the one hand, the distinguishable time interval Δt is as small as 0.11 μs, which is reduced by 72.5% compared to the pulse width t_p=0.4 μs. On the other hand, the full-width at half-maximum (FWHM) for the flaw tip in B-scan image is decreased significantly by Sparse-SAFT. Figure 9 presents the transverse profile graphs corresponding to the lower tip of the artificial defect in the different reconstructed images. The measured FWHM in Figure 9(b)

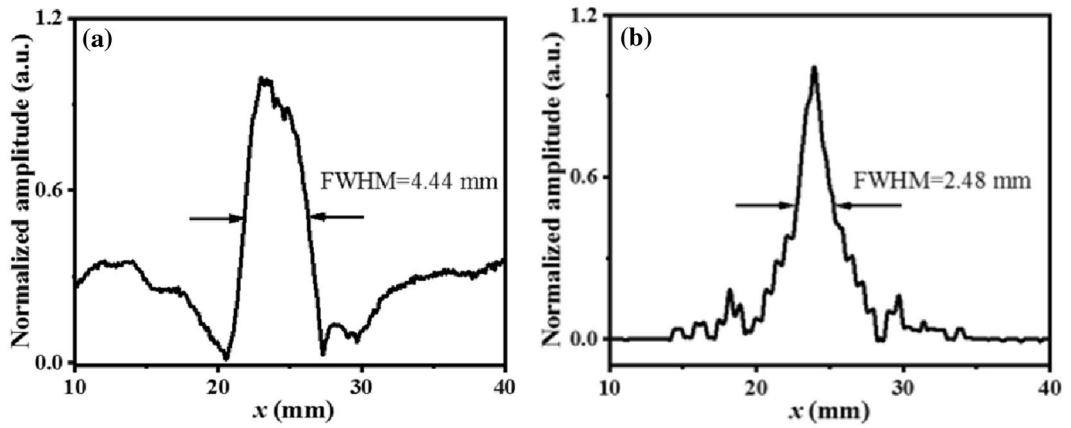

Figure 9 Transverse profile graphs corresponding to the lower tip of the artificial defect in different reconstructed images: (**a**) SAFT image, (**b**) Sparse-SAFT image

is 44% of that in Figure 9(a) processed by conventional SAFT, i.e., the lateral resolution is improved by 56%.

Simulated and experimental results indicate that Sparse-SAFT is suitable for identifying shallow subsurface defects by enhancing image resolution. Meanwhile, the small defects beyond dead zone can also be detected by Sparse-SAFT. Figure 10(a) presents another artificial defect with a height of 3.0 mm at the depth of 11.0 mm in carbon steel specimen. Two 5.0 MHz probes with 52.0 mm PCS are adopted to perform ultrasonic TOFD inspection. The original B-scan image and reconstructed image by Sparse-SAFT are shown in Figure 10(b) and (c), respectively. The time resolution and lateral resolution are enhanced significantly by Sparse-SAFT, and the time differences Δt_1=0.76 μs and Δt_2=1.23 μs are obtained from Figure 10(c). The calculated flaw depth and height are respectively equal to 11.0 and 3.2 mm, whose relative errors are no more than 6.7%.

5 Conclusions

(1) Sparse-SAFT is proposed by combining sparse deconvolution and SAFT to weaken the influence of pulse width and beam spreading on the time resolution and lateral resolution in TOFD imaging.
(2) Simulated and experimental results demonstrate that the time resolution and lateral resolution are respectively enhanced by 72.5% and 56% with Sparse-SAFT compared to conventional SAFT.

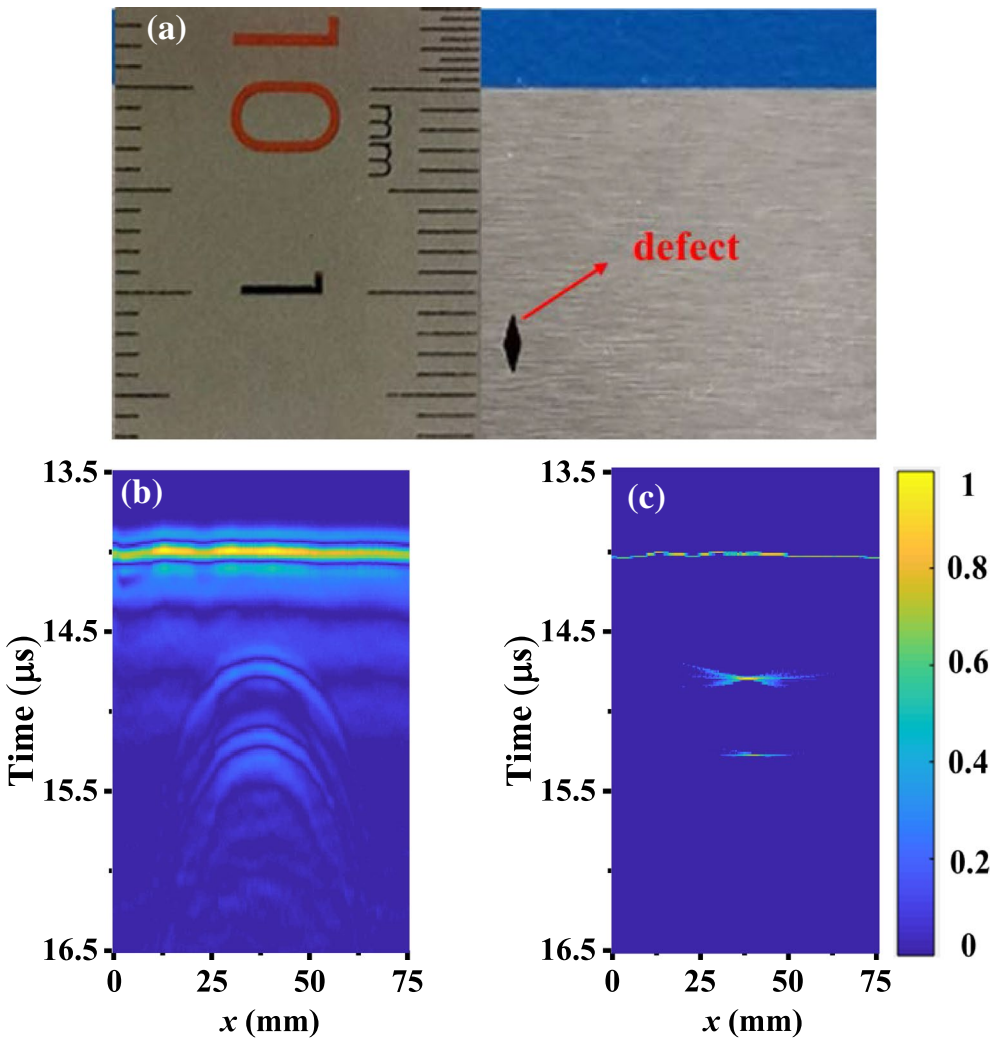

Figure 10 Carbon steel specimen and TOFD images: (**a**) carbon steel specimen with an artificial defect beyond dead zone, (**b**) original TOFD B-scan image, (**c**) reconstructed image by Sparse-SAFT

(3) The depths and heights of the defects located in and beyond dead zone are determined by Sparse-SAFT with no more than 10.3% measurement error.

Acknowledgements
Not applicable.

Author Contributions
XS wrote the draft manuscript and conducted experiment; LL and SJ were in charge of the whole trial. All authors read and approved the final manuscript.

Authors' Information
Xu Sun, is currently a PhD candidate at *School of Materials Science and Engineering*, *Dalian University of Technology*, *China*. His research interests include ultrasonic signal processing.
Li Lin, is currently a Professor at *School of Materials Science and Engineering*, *Dalian University of Technology*, *China*. Her main research interests include nondestructive testing and evaluation for materials.
Shijie Jin, is currently an associate professor at *School of Materials Science and Engineering*, *Dalian University of Technology*, *China*. His research interests include nondestructive testing and evaluation for materials.

Funding
Supported by National Key Research and Development Program of China (Grant No. 2019YFA0709003), National Natural Science Foundation of China (Grant No. 51905079), Liaoning Revitalization Talents Program (Grant No. XLYC1902082).

Competing Interests
The authors declare no competing financial interests.

Received: 30 October 2021 Revised: 14 April 2022 Accepted: 22 June 2022
Published online: 16 July 2022

References

[1] H Song, Y Yang. Super-resolution visualization of subwavelength defects via deep learning-enhanced ultrasonic beamforming: A proof-of-principle study. *NDT & E International*, 2020, 116: 102344.
[2] B W Drinkwater, P D Wilcox. Ultrasonic arrays for non-destructive evaluation: A review. *NDT & E International*, 2006, 39(7): 525-541.
[3] S J Jin, X Sun, Z B Luo, et al. Quantitative detection of shallow subsurface cracks in pipeline with time-of-flight diffraction technique. *NDT & E International*. 2021, 118: 102397.
[4] S J Jin, X Sun, T T Ma, et al. Quantitative detection of shallow subsurface defects by using mode-converted waves in time-of-flight diffraction technique. *Journal of Nondestructive Evaluation*, 2020, 39(2): 1-8.
[5] K Nakahata, K Karakawa, K Ogi, et al. Three-dimensional SAFT imaging for anisotropic materials using photoacoustic microscopy. *Ultrasonics*, 2019, 98: 82-87.
[6] J Duan, L Luo, X Gao, et al. Hybrid ultrasonic TOFD imaging of weld flaws using wavelet transforms and image registration. *Journal of Nondestructive Evaluation*, 2018, 37(2): 1-11.
[7] M Spies, H Rieder, A Dillhöfer, et al. Synthetic aperture focusing and time-of-flight diffraction ultrasonic imaging—past and present. *Journal of Nondestructive Evaluation*, 2012, 31(4): 310-323.
[8] D Z Chi, T Gang. Shallow buried defect testing method based on ultrasonic TOFD. *Journal of Nondestructive Evaluation*, 2013, 32(2): 164-171.
[9] Z Wang, Y Zhou, J Tian. TOFD-scan imaging based on synthetic aperture focusing technique. *17th World Conference on Nondestructive Testing*, Shanghai, China, 2008: 25-28.
[10] A N Sinclair, J Fortin, B Shakibi, et al. Enhancement of ultrasonic images for sizing of defects by time-of-flight diffraction. *NDT & E International*, 2010, 43(3): 258-264.
[11] F Honarvar, H Sheikhzadeh, M Moles, et al. Improving the time-resolution and signal-to-noise ratio of ultrasonic NDE signals. *Ultrasonics*, 2004, 41(9): 755-763.
[12] G Hayward, J E Lewis. Comparison of some non-adaptive deconvolution techniques for resolution enhancement of ultrasonic data. *Ultrasonics,* 1989, 27(3): 155-164.
[13] X Sun, S J Jin, D H Zhang, et al. Suppression of dead zone in TOFD with autoregressive spectral extrapolation. *Journal of Mechanical Engineering*, 2018, 54(22): 15-20. (in Chinese)
[14] R Hou, Y Xia, Y Bao, et al. Selection of regularization parameter for l_1-regularized damage detection. *Journal of Sound and Vibration*, 2018, 423: 141-160.
[15] Y Chang, Y Zi, J Zhao, et al. An adaptive sparse deconvolution method for distinguishing the overlapping echoes of ultrasonic guided waves for pipeline crack inspection. *Measurement Science & Technology*, 2017, 28(3): 35002.
[16] H Jin, K Yang, S Wu, et al. Sparse deconvolution method for ultrasound images based on automatic estimation of reference signals. *Ultrasonics*, 2016, 67: 1-8.
[17] C Soussen, J Idier, E Carcreff, et al. Ultrasonic nondestructive testing based on sparse deconvolution. *Journal of Physics* (*Conference Series*), 2012, 353(12018): 12010-12018.
[18] F Boßmann, G Plonka, T Peter, et al. Sparse deconvolution methods for ultrasonic NDT: Application on TOFD and wall thickness measurements. *Journal of Nondestructive Evaluation,* 2012, 31(3): 225-244.
[19] X Sun, L Lin, Z Ma and S Jin. Enhancement of time resolution in ultrasonic time-of-flight diffraction technique with frequency domain sparsity-decomposability inversion (FDSDI) method. *IEEE Transactions on Ultrasonics, Ferroelectrics, and Frequency Control*, 2021, 68(10): 3204-3215.
[20] T Olofsson, E Wennerstrom. Sparse deconvolution of B-scan images. *IEEE Transactions on Ultrasonics, Ferroelectrics and Frequency Control,* 2007, 54(8): 1634-1641.
[21] X W Shen, H W Hu, X B Li, et al. Study on PCA-SAFT imaging using leaky Rayleigh waves. *Measurement*, 2021, 170: 108708.
[22] L Li, K Jiang, F Li. Research on defect image enhancement in ultrasonic TOFD detection. *The Open Cybernetics & Systemics Journal*, 2015, 9(1): 464-472.
[23] M Li, Y Tseng, P Wang. Improved synthetic aperture focusing technique for acoustic-resolution photoacoustic microscopy. *IEEE Ultrasonics Symposium*, Orlando, FL, USA, 2011: 2384-2387.
[24] M Spies, H Rieder. Synthetic aperture focusing of ultrasonic inspection data to enhance the probability of detection of defects in strongly attenuating materials. *NDT & E International*, 2010, 43(5): 425-431.
[25] A Shlivinski, K J Langenberg. Defect imaging with elastic waves in inhomogeneous-anisotropic materials with composite geometries. *Ultrasonics*, 2007, 46(1): 89-104.
[26] Y Li, Z Wang, Y Zhang, et al. Synthetic aperture imaging in cylindrical component using ultrasonic immersion forward vector algorithm. *Russian Journal of Nondestructive Testing*, 2020, 56(5): 397-407.
[27] T Gang, D Chi, Y Yuan. Ultrasonic TOFD technique and image enhancement based on synthetic aperture focusing technique. *Transactions of the China Welding Institution*, 2006, 27(10): 7-11. (in Chinese)
[28] Y Chen, Q Mao, W Shi, et al. Research on ultrasonic TOFD imaging inspection for heavy-walled weld based on phase coherence characteristics. *Journal of Mechanical Engineering*, 2019, 55(4): 25-32. (in Chinese)
[29] Q Han, P Wang, H Zheng. Modified ultrasonic time-of-flight diffraction testing with Barker code excitation for sizing inclined crack. *Applied Acoustics*, 2018, 140: 153-159.
[30] S G Haslinger, M J S Lowe, Z Wang, et al. Time of flight diffraction for rough planar defects. *NDT & E International*, 2021, 124: 102521.
[31] Z H Chen, G L Huang, C Lu, et al. Automatic recognition of weld defects in TOFD D-scan images based on faster R-CNN. *Journal of Testing and Evaluation,* 2018, 48(2): 1-14.
[32] S Kim, K Koh, M Lustig, et al. An Interior-Point Method for Large-Scale l_1-Regularized Least Squares. *IEEE Journal of Selected Topics in Signal Processing*, 2007, 4(1): 606-617.
[33] S Q Shi, L Lin, Z B Luo, X Sun, S J Jin. Resolution enhancement of ultrasonic imaging at oblique incidence by using WTFM based on FMC-AR. *Measurement*, 2021,183:109798.